

DOI: 10.1002/ ((please add manuscript number))

**Article type:** Full Paper

**Electrical Conductivity Adjustment for Interface Capacitive-like Storage in Sodium-ion Battery**

*Qianwen Li, Hang Wang, Xinfeng Tang, Min Zhou\*, Huaping Zhao, Yang Xu, Wei Xiao, Yong Lei\**

Dr. Q. Li

College of Light-Textile Engineering and Art, Anhui Agriculture University, Hefei, 230036, P. R. China

Dr. Q. Li, Dr. H. Zhao, Prof. Y. Lei

Institute of Physics and Macro- and Nanotechnologies MacroNano® (IMN & ZIK), Ilmenau University of Technology, Ilmenau, 98693, Germany

E-mail: yong.lei@tu-ilmenau.de

Mr. H. Wang, Mr. X. Tang, Prof. M. Zhou

Hefei National Laboratory for Physical Sciences at the Microscale, School of Chemistry and Materials Science, University of Science and Technology of China, Hefei, Anhui 230026, P. R. China

E-mail: mzchem@ustc.edu.cn

Dr. Y. Xu

Department of Chemistry, University College London, UK WC1H 0AJ

W. Xiao

Electronic Measurements Research Laboratory, Ilmenau University of Technology, Ilmenau, 98693, Germany

**Keywords:** eletrodes, 3D current collector, electrical conductivity, interface capacitive-like storage, batteries

Sodium ion battery (SIB) is significant for grid-scale energy storage. However, large radius of Na ions raises the difficulties of ion intercalation, hindering the electrochemical performance during fast charge/discharge. Conventional strategies to promote rate performance focus on the optimization of ion diffusion. Improving interface capacitive-like storage by tuning the electrical conductivity of electrodes is also expected to combine the features of high energy density of batteries and high power density of capacitors. Inspired by this concept, an oxide-metal sandwich three-dimensional ordered macroporous architecture (3DOM) stands out as a superior anode candidate for high-rate SIBs. Taking Ni-TiO<sub>2</sub> sandwich 3DOM as proof-of-concept, anatase TiO<sub>2</sub> delivers a reversible capacity of 233.3 mAh g<sup>-1</sup> in half-cells and 210.1 mAh g<sup>-1</sup> in full-cells after 100 cycles at 50 mA g<sup>-1</sup>. At the high charge/discharge rate of 5000 mA g<sup>-1</sup>, 104.4 mAh g<sup>-1</sup> in half-cells and 68 mAh g<sup>-1</sup> in full-cells can also be obtained with satisfied stability. In-depth analysis of electrochemical kinetics evidences that the remarkable sodium storage ability origins from dominated interface capacitive-like storage, which enables ultrafast uptaking and releasing of Na-ions. This understanding between electrical conductivity and rate performance of SIBs is expected to guild the future design to realize effective energy storage.

## 1. Introduction

To solve the resulting problems of fossil fuel burning, the conversion and utilization of clean renewable energy are of high significance. Owing to the imminent and unpredictable features of such resources, energy storage technologies have thus attracted intensive attention for both basic research and practical industry.<sup>[1]</sup> Among them, lithium ion battery (LIB) stands out as a prominent energy storage technology with high potential of large-scale off-grid applications.<sup>[2]</sup> However, issues like the accessible lithium, safety and cost inspire us to find other alternatives.<sup>[3]</sup> Since sodium not only shares similar electrochemical properties with lithium, but also possesses several advantages like abundant resources, high safety and low cost, sodium-ion battery (SIB) has thus been considered as a promising candidate for energy storage.<sup>[4]</sup> Many researchers have devoted into corresponding studies of electrode materials, especially in pursuit of satisfied rate performance that is even more important due to the demands of fast charge/discharge.<sup>[5]</sup> The promising methods without consuming reversibility still remain a challenge to Na-free transition metal oxide anode materials with intercalation mechanism.<sup>[6]</sup>

In general, ion intercalation contains three steps during cycles: solvated Na<sup>+</sup> diffusion within the electrolyte; charge-transfer reactions at or near the interface between active materials and electrolyte; Na<sup>+</sup> diffusion in the bulk materials. Hence, the whole ability of sodium storage is attributed to both Na-ion intercalation in bulk and capacitance at or near the interface. Larger radius of Na<sup>+</sup> (1.02 Å) vs. Li<sup>+</sup> (0.76 Å) always raises more complex requirements for electrode materials' crystalline structures during bulk intercalation,<sup>[6]</sup> which would largely hinder the performance at high charge/discharge rates. Interface capacitive-like storage always occurs on the order of seconds and minutes, and thus the motivation from increased interface capacitive-like storage is expected to well balance high capacity and high rate performance in the same

material.<sup>[7]</sup> Moreover, interface capacitive-like storage will not result in a huge change of crystalline structures, which would also contribute to the stability during long-term sodium storage.

Several methods, like defects or amorphization engineering of materials' crystalline structures<sup>[8]</sup> and morphology optimization,<sup>[9]</sup> have been used to enhance the rate performance from improved interface capacitive-like storage and obtained some preliminary results. Deep understanding of interface capacitive-like storage nature would be helpful for developing clear criteria for intercalation-based electrodes. Since the contributions at or near the interface are mainly controlled by surface instead of diffusion, and always accompanied with electron transfer or hopping,<sup>[10]</sup> sufficient electrical conductivity for fast electron movement might be also significant to add extra capacitive-like sodium storage at or near the interface.<sup>[11]</sup> This enhancement would be expected to benefit for high-rate charge/discharge in short time.

Inspired by this understanding, an active material-metal current collectors and sandwich architecture is an effective candidate to shorten electron transport paths throughout the entire electrode, originated from high electrical conductivity of metal skeleton. To evidence this concept more clearly, we chose anatase TiO<sub>2</sub>, a typical intercalation-based material with unsatisfactory rate performance, as an example of active materials. It is facile to deposit TiO<sub>2</sub> uniformly on complex conductive metal skeletons with uniform thickness through suitable approaches, such as atomic layer deposition (ALD).<sup>[12]</sup> Considering the requirements of electrolyte infiltration and volume expansion accommodation of active materials, a 3D ordered microporous architecture (3DOM) is selected as a skeleton candidate. First, interconnected periodic microporous architectures can provide quasi-1D long-range ordered paths for electron transport throughout the entire electrode, and further enhance the electric conductivity and long-term stability of overall electrodes at the same time. The resulting sandwich architecture

consists of uniform anatase  $\text{TiO}_2$  and 3DOM Ni skeleton without any additives and binders. Clean interface of active material can efficiently exclude the influences of other phases. Second, 3DOM is incorporated with dual porosity, resulting from controllable templates with plasticity of the diameter and the interconnected area between neighboring spheres, respectively. It is expected to increase the area of electrode/electrolyte junction and electrode/current collector junction. Third, with the help of ALD techniques, it is facile to control the thickness of  $\text{TiO}_2$  in samples with and without Ni skeleton. So, both architectures are quite similar through concise control of ALD, resulting in the same mass loading and ion diffusion length, but different electrical conductivity. It is helpful to focus on the relationship among electric conductivity, interface capacitive-like storage and rate performance.

As expected, the Ni- $\text{TiO}_2$  sandwich 3DOM deliveries great rate performance during sodium storage of both half-cells and full-cells. A reversible capacity of  $233.3 \text{ mAh g}^{-1}$  in half cells and  $210.1 \text{ mAh g}^{-1}$  in full cells (coupled with  $\text{P2-Na}_{2/3}\text{Ni}_{1/3}\text{Mn}_{2/3}\text{O}_2$  cathode) can be obtained after 100 cycles at  $50 \text{ mA g}^{-1}$ . Moreover, at the high charge/discharge rate of  $5000 \text{ mA g}^{-1}$ ,  $\text{TiO}_2$  can deliver specific capacities of  $104.4 \text{ mAh g}^{-1}$  in half cells and  $68 \text{ mAh g}^{-1}$  in full cells with satisfied stability. Such enhancement originates primarily from 3DOM Ni skeleton, which can not only serve as the supporter for anatase  $\text{TiO}_2$ , but also provide direct and reduced pathways for electron transport, leading to boosted interface capacitive-like storage. Our results confirm the possibilities of employing electrical conductivity adjustment of electrodes to improve interface capacitive-like storage for effective high-rate energy storage. This observation is expected for a universal design to realize satisfied energy storage using other large transport ions.

## 2. Results and Discussion

### 2.1. Fabrication and characterizations of Ni-TiO<sub>2</sub> sandwich 3DOMs.

To realize this tentative idea of the active material-current collector sandwich 3DOM architecture, it is of great significance to find feasible and straightforward procedures. Being a technologically facile approach, colloidal crystal template (CCT) method assisted by atomic layer deposition (ALD) is a promising candidate to fabricate the sandwich 3DOMs. The schematic fabrication process is shown in **Scheme 1**. Polystyrene (PS) spheres with the same diameter were first assembled on a conductive substrate to construct a large-scaled CCT. Then the interstices in CCT were filled with metal to generate an in-situ 3DOM conductive skeleton after removing PSs. Finally, the active materials, like oxides, were uniformly coated on the metal skeleton by ALD to obtain the final sandwich 3DOMs.

To confirm aforementioned steps, we choose Ni as the metal skeleton and anatase TiO<sub>2</sub> as the active material. **Figure 1a** and **1b** show the representative scanning electron microscope (SEM) images of 3DOM Ni skeleton and Ni-TiO<sub>2</sub> sandwich 3DOM, which are the replica translated from the periodic CCTs based on PSs with ~500 nm diameter. The Ni skeleton with the periodic macroporous structure were obtained on Ti foil after the electrochemical deposition and template removal by organic solvents. And then ~20 nm TiO<sub>2</sub> was deposited on Ni skeleton to form an oxide-metal sandwich 3DOM structure, followed by annealing to obtain anatase phase. As shown in Figure 1b, morphologies of both surface layer and inner layers (highlighted in the circle of Figure 1b) confirm the successful realization of Ni-TiO<sub>2</sub> sandwich 3DOM, the phase and purity of which were further examined by X-ray diffraction (XRD) in Figure 1c and Raman spectroscopy in Figure 1d. Besides the diffraction peaks from Ni (JCPDS No. 65-2865) and Ti (JCPDS No. 44-1294) substrates, all the other peaks can be indexed to the diffractions of tetragonal anatase TiO<sub>2</sub> (JCPDS No. 21-1272). No peaks of other phases can be detected,

indicating the high purity of the as-prepared Ni-TiO<sub>2</sub> sandwich 3DOMs. The Raman scattering spectra of as-fabricated samples further evidences the purity of anatase TiO<sub>2</sub> based on vibration modes of A<sub>1g</sub>, B<sub>1g</sub>, E<sub>g</sub>.<sup>[13]</sup> It is worth mentioning that there is no peak in Raman spectra between 1200 and 1800 cm<sup>-1</sup>, where the D band and the G band of carbonaceous materials appears. Two symmetrical peaks in X-ray photoelectron spectroscopy (XPS) are attributed to +4 state of Ti<sup>4+</sup> in the lattice as shown in **Figure S1**.<sup>[1c,8a]</sup> Overall, we can infer that no carbon is contained in the Ni-TiO<sub>2</sub> sandwich 3DOMs.<sup>[14]</sup>

To clearly visualize the sandwich 3DOM features in large scale, transmission electron microscopy (TEM) analysis and energy-dispersive X-ray spectroscopy (EDX) scan were used here to verify the distributions of Ni, Ti and O (**Figure 2a-2d**) using samples with templates consisted of 100 nm diameter spheres. TEM image shown in Figure 2a evidences the periodic microporous features of the entire Ni-TiO<sub>2</sub> sample. The elemental distribution of Ni (Figure 2b) exhibits similar 3DOM morphology compared with that of Ni-TiO<sub>2</sub> sample, confirming the core of 3DOM Ni skeleton, while Ti and O are distributed around the Ni skeleton uniformly like a sandwich construction. With the help of color code, the clean interface between Ni (orange) and TiO<sub>2</sub> (blue) can be clearly found in high resolution TEM (HRTEM) image (Figure 2e), verifying the direct contact between the active materials and current collectors. No other impurities like NiO, carbon exist in the sandwich interface. Summarizing 3DOM, where a 3D macroporous conductive network is formed by the metal Ni with uniform coating of anatase TiO<sub>2</sub> acted as active materials on both sides. To better illuminate the structure information, enlarged HRTEM images of Ni and TiO<sub>2</sub> are shown in Figure S2.

## 2.2. Electrochemical characteristics of Ni-TiO<sub>2</sub> sandwich 3DOMs.

To quantify the sodium storage of Ni-TiO<sub>2</sub> sandwich 3DOM, we first employ a half-cell configuration with TiO<sub>2</sub>-based working electrode and Na disk counter electrode to assemble

two-electrode coin cells. In order to demonstrate our hypothesis of the influences of electrical conductivity of electrodes, anatase TiO<sub>2</sub> 3DOM without Ni skeleton was fabricated as reference samples with same thickness of TiO<sub>2</sub> (2×20 nm) and mass loading. Corresponding characterizations can be found in **Figure S3**. Since both kinds of 3DOMs were fabricated directly on the conductive Ti substrates, we didn't use any conductive additive and polymeric binder to ensure sufficient conductivity of entire electrodes. Hence, all the exhibited sodium storage abilities only originate from electrochemical behaves of anatase TiO<sub>2</sub> with comparatively clean surface. Cyclic voltammetry (CV) measurements were first carried out to elucidate the redox processes in host matrix with different constructions. To avoid the disturbance from solid electrolyte interphase (SEI) layer and the other irreversible reactions, the second cycle of CV curves is chosen as diagrammed in **Figure 3a**. Looking carefully into the appearances of both CV curves, the pair of redox peaks located at approximately 0.67 V (cathodic) and 0.85 V (anodic) are observed in both Ni-TiO<sub>2</sub> sandwich 3DOM and TiO<sub>2</sub> 3DOM. This redox pair well matches the potential of reversible Ti<sup>4+</sup>/Ti<sup>3+</sup> redox coupled with Na<sup>+</sup> insertion and extraction into anatase TiO<sub>2</sub>.<sup>[15]</sup> Considering similar mass loading of Ni-TiO<sub>2</sub> sandwich 3DOM and TiO<sub>2</sub> 3DOM without Ni skeleton, it is reasonable to exclude the influence of the mass of the active material without normalization of Y-axis. We can further assert that the electrochemical behaves during Faradaic bulk storage of sodium is quite similar during low charge/discharge by similar location of redox pairs. Gradually broadening curves of Ni-TiO<sub>2</sub> sandwich 3DOM may indicate larger contributions from interface capacitive-like storage.<sup>[9d, 16]</sup> Hence, Ni-TiO<sub>2</sub> sandwich 3DOM exhibits larger capacities during cycles, the value of which keeps 233 mAh·g<sup>-1</sup> even after 100 cycles at the low charge/discharge rate of 50 mA g<sup>-1</sup>, while TiO<sub>2</sub> 3DOM only contributes a capacity of 175 mAh g<sup>-1</sup> (Figure 3b). The results can be further verified by charge/discharge profiles of Ni-TiO<sub>2</sub> sandwich 3DOM and TiO<sub>2</sub> 3DOM at the 1st, 2nd, 20th and 50th cycle at the current density of 50 mA g<sup>-1</sup> in Figure 3c and 3d. In accordance

with CV data, the appearances of discharge curves also infer that the electrochemical contributions related to the intercalation reactions in bulk together with interface capacitive-like storage. The former storage mainly contributes to the capacities within discharge plateau, while the other capacities are mainly attributed to capacitive-like storage.

As mentioned before, one of key challenges within SIBs is to enable high capacity and high power at the same time. To examine this potential, the rate capabilities were recorded in **Figure 4a** together with corresponding charge/discharge profiles in **Figure S4** to investigate the feasibility of fast charge/discharge. Ni-TiO<sub>2</sub> sandwich 3DOM shows discharge capacities of 280, 193, 135, 120 and 105 mAh g<sup>-1</sup> at the current densities of 50, 200, 1000, 2000 and 5000 mA g<sup>-1</sup>, while the values of TiO<sub>2</sub> 3DOM are 216, 139, 86, 63 and 47 mAh g<sup>-1</sup>, respectively. Besides the high capacities at high rates, the retention reaches 91% from the 2nd cycles to 1000th cycles at the current density as high as 2000 mA g<sup>-1</sup> (Figure 4b). The specific capacity after 1000 cycles can still reach 109 mAh g<sup>-1</sup>, near 1-fold larger than that of TiO<sub>2</sub> 3DOM. It implies that high-rate sodium storage of Ni-TiO<sub>2</sub> sandwich 3DOM is feasible, reversible and stable. Comparison with other current collectors with different geometry, like highly ordered Ni core-shell nanowire array, <sup>[19c]</sup> randomly oriented Ni nanowire array, <sup>[19c]</sup> planar morphology as shown in **Figure S5 and S6**, Ni 3DOM skeleton serves as an excellent candidate for 3D current collector. Ascended a survey of literatures, our results of SIBs stand out among various pure TiO<sub>2</sub>-based anodes. Related comparison with previous TiO<sub>2</sub>-based anodes can be seen in **Figure S7** for rate capacities and **Table S1** for retention in details.

### 2.3 In-depth discussion of electrochemical behaviors.

To deeply understand the origins of rate performance gap between Ni-TiO<sub>2</sub> sandwich 3DOM and TiO<sub>2</sub> 3DOM, here, four important points should be first predeclared considering the electrochemical behaviors. (i) According to Raman spectra in Figure 1d, there is no peak found

in the range from 1200 to 1800  $\text{cm}^{-1}$ , which might be assigned to the signals of carbonaceous materials. We also cannot find any peak belonged to various oxidation products of Ni, which is further convinced by XRD and HRTEM results in Figure 1c and Figure 2e. Meanwhile, we haven't added any conductive additive and polymeric binder within all the electrodes. Hence, all the electrodes don't contain any carbonaceous material with the potential to change the long-term stability and rate performance.<sup>[17]</sup> The entire gap of sodium storage ability at different rates should be only attributed to the electrodes themselves. (ii) The thickness of  $\text{TiO}_2$  in both architectures are quite similar through concise control of ALD, resulting in the same mass loading and ion diffusion length as show in Scheme 2. Related impacts from ion diffusion can be excluded. (iii) Both kinds of electrodes are fabricated by topologic transformation from CCTs, so the morphology features are similar. We can fully exclude related influences from electrode architectures like facet, orientation, etc.<sup>[18]</sup> It is worth mentioning that  $\text{TiO}_2$  sandwich 3DOM even possesses less contact area with electrolyte than  $\text{TiO}_2$  3DOM because of the existence of Ni skeleton and the requirements of same ion diffusion length, which would slightly decrease the ability of interface storage in a conventional sense. (iv) Both kinds of electrodes are stored in  $\text{N}_2$  before measurement. It is not necessary to take the detrimental influences from surface state by absorption and/or adhesion into account. After such careful analysis of the two architectures, the major difference between the two kinds of electrodes is the existence of Ni 3DOM current collector instead of planar current collector. Hence, we turn our attention to electron transport that might result in huge change of rate performance of SIBs. Shown in **Figure 5a** are the current-voltage (I-V) characteristics of Ni- $\text{TiO}_2$  sandwich 3DOM and  $\text{TiO}_2$  3DOM. The symmetrical and linear appearance of I-V curves indicate the Ohmic contacts between the electrode and conductive substrate.<sup>[19]</sup> Obviously, the existence of Ni 3DOM skeleton indeed largely facilitates electron transport and reduces the resistance

throughout the whole matrix by 20 folds. Facile electron transport leads to decreased charge-transfer resistance ( $R_{ct}$ ) at surface. According to a modified Randles equivalent circuit in **Figure S8**, analysis of Nyquist plots of electrochemical impedance spectroscopy (EIS) ranging from 100k Hz to 0.1 Hz (Figure 5b, 5c) confirms decreased  $R_{ct}$  after introducing the Ni 3DOM current collector (Figure 5d). And the gap of  $R_{ct}$  becomes larger with increased cycles. Since  $R_{ct}$  mainly depends on the charge transfer resistance related to the redox reactions across the electrode/electrolyte interface,<sup>[20]</sup> smaller  $R_{ct}$  suggests much facile reactions and associated sodium storage near or at interface.

This understanding inspires us to think over a question: how can we associate electrical conductivity of electrodes with SIB performance at high rates? Due to the same active materials, the accommodation ability of Na ions is the same in theory. So, we try to hunt for the origins based on the possible kinetic factors. Cyclic voltammetry (CV) is a powerful tool to illuminate the electrochemical kinetics of the electrodes towards  $\text{Na}^+$ . Current response to an applied sweep rate will vary depending on whether the redox reaction is diffusion-controlled or not.<sup>[10b, 11a, 21]</sup> Hence, we recorded the CV curves of electrodes before and after the introduction of Ni 3DOM current collector at various scan rates from 0.1 to 5  $\text{mV s}^{-1}$  (**Figure 6a** and **6b**). Similar redox pairs also match the potentials of reversible  $\text{Ti}^{4+}/\text{Ti}^{3+}$  redox, consistent with the conclusions from Figure 3a. In general, ion intercalation contains three steps: solvated  $\text{Na}^+$  diffusion within the electrolyte; charge-transfer reactions at or near the interface between active materials and electrolyte; and Na-ion diffusion in the bulk materials. According to the features of these electrochemical behaves, there are two types of contributions towards the whole sodium storage: Na-ion intercalation in bulk related to diffusion-controlled mechanism and capacitance at or near the interface free of diffusion-controlled mechanism. To visualize the

storage mechanism, we seek for the helps from the relationship of peak current ( $i$ ) and scan rate ( $v$ ) by the following Equations (1-2):

$$i = av^b \quad (1)$$

$$\log(i) = b\log(v) + a \quad (2)$$

Here,  $a$  and  $b$  are adjustable constants.  $b$ -value can be obtained from the slopes by plotting  $\log(i)$  against  $\log(v)$ .  $b$ -value should be 0.5 provided the sodium storage is an ideal faradaic intercalation process controlled by semi-infinite linear diffusion, whereas the  $b$ -value of 1.0 stands for a pure capacitive contribution without diffusion control.<sup>[22]</sup> As depicted in Figure 6c and 6d, both kinds of electrodes display a good linear relationship. The  $b$ -values of Ni-TiO<sub>2</sub> sandwich 3DOM are 0.92 and 0.91 for anodic and cathodic processes, respectively, which are closer to 1 than those of TiO<sub>2</sub> 3DOM (0.83 and 0.80 for anodic and cathodic processes). This value is closed to amorphous TiO<sub>2</sub> 3DOM with mainly surface-controlled capacitive-like contributions during charge/discharge.<sup>[8a,15a]</sup> Such comparison implies that the sodium storage is less diffusion controlled after the introduction of Ni 3DOM current collector. It is a strong evidence that facile electron transport resulted from Ni 3DOM current collector can change the electrochemical kinetics and promote the fast interface capacitance-like sodium storage free of diffusion control.

Hence, the interface capacitance-like contribution at a certain scan rate ( $v$ ) can be further quantitatively differentiated by separating current response ( $i$ ) at a fixed potential into bulk Na-ion intercalation contribution and interface capacitance-like contribution according to Equation (3):

$$i = k_1v + k_2v^{1/2} \quad (3)$$

Here,  $k_1$  and  $k_2$  are adjustable constants. Solving for their values at each potential is helpful for the separation of the diffusion-controlled currents and capacitive-like currents, because the former one is proportional to  $v$ , while the latter one is proportional to  $v^{1/2}$ .<sup>[11b, 21c, 22a]</sup> **Figure 7a-7f** exhibit the typical CV curves for the capacities from interface capacitance-like contributions (green region) in comparison with the total capacities at the scan rates of 0.2, 1 and 4  $\text{mV s}^{-1}$ , respectively. It is obvious to find the quantified results that the interface capacitance-like contribution gradually improves with the accelerated scan rates. At the scan rate of 0.2  $\text{mV s}^{-1}$ , ~63.7% of the total capacity is capacitive in nature. The ratio increases to 90.4% with the improved scan rate to 4  $\text{mV s}^{-1}$ . More importantly, the Ni-TiO<sub>2</sub> sandwich 3DOM possesses much larger interface capacitance-like contributions than TiO<sub>2</sub> 3DOM. The interface capacitance-like contribution is only 79.2 % of the total sodium ability at 4  $\text{mV s}^{-1}$ . Considering the four prerequisites, all the results indicate that facile electron transport by introducing Ni 3DOM current collector can successfully promote the interface capacitance-like sodium storage.

In general, there are four major electron movement events occurring during ion-intercalation and deintercalation as depicted by the white arrays in **Scheme 2**: (1) accumulation and/or reaction at the electrode/electrolyte interface; (2) electron transport throughout the electrode; (3) electron injection and extraction at the electrode-current collector interface; (4) electron transport in current collector. According to previous analysis, comparatively small surface area may slightly weaken the electron utilization at surface because of a little less accessibility of the active material for Na<sup>+</sup>. But the existence of Ni 3DOM current collector can obviously shorten electron transport pathways in step (2) (within active materials) and amplified the contact area of electrode-current collector interface as shown in Scheme 2. Since electron transport in current collector is much faster than that in materials and across the interface, this

amelioration in the latter two points can largely improve the electron transport and reduce the resistance throughout the entire electrodes, associated with facile interface charge transfer evidenced in Figure 5. As well known, electron movement is completed by a redox reaction in the materials, and thus is much faster than ion diffusion. Hence, optimization of ion diffusion dominates the previous studies. However, accelerated electron transport would also play a vital role on ion transfer at the interface between the material and electrolyte, which has been regarded as a slow process during the electrochemical energy storage.<sup>[11b, 15a]</sup> 3DOM metal skeleton can not only serve as supporter for active materials, but also provides a direct and reduced way for electron transport. First, fast electron transport can avoid the charge accumulation at and/or near the interface, leading to accelerated interface kinetics and decreased potential of meaningless side reactions. Second, fast rearrangement of lattice at the interface can be realized by facile electron supplement or removal. Third, high electronic conductivity can reduce the electrostatic repulsive force, which would fasten the electron transfer and transport in particular on the interface. Overall, the processes of interface capacitive-like storage, like pseudo-capacitance or double layer capacitance, can both be optimized together with the ion intercalation/deintercalation of  $\text{Na}^+$ . Interface capacitive-like storage always occurs on the order of seconds and minutes, and thus promoted interface capacitive-like storage is particularly expected to improve high-rate capacities in short time.<sup>[11a]</sup> Moreover, interface capacitive-like storage will not result in a huge change of crystalline structures that can be recovered fast. This would benefit for well balance of high capacity and high-rate performance at the same time. Hence, it is efficient and significant to employ the sandwich design to largely boost rate performances of SIBs by tuning the electrical conductivity of electrodes.

#### **2.4 Full-cell electrochemical characteristics of Ni-TiO<sub>2</sub> sandwich 3DOMs.**

Such superiorities can also be used to improve the rate performance in full cells. To check this potential, layered P2- $\text{Na}_{2/3}\text{Ni}_{1/3}\text{Mn}_{2/3}\text{O}_2$  is chosen as cathode to assemble two-electrode full cells together with Ni-TiO<sub>2</sub> sandwich 3DOM and TiO<sub>2</sub> 3DOM anodes like the scheme in **Figure 8a**. Corresponding characterizations and electrochemical performance of P2- $\text{Na}_{2/3}\text{Ni}_{1/3}\text{Mn}_{2/3}\text{O}_2$  are listed in **Figure S9**. Similar to the superior performance in half cells, Ni-TiO<sub>2</sub> sandwich 3DOM shows a long-term stability and large sodium storage as shown in Figure 8b and 8c. With respect to the mass of anodes, a capacity of  $\sim 210.1 \text{ mAh g}^{-1}$  can be obtained even after 100 cycles at  $50 \text{ mA g}^{-1}$ , the value of which is much larger than TiO<sub>2</sub> 3DOM anode and amorphous TiO<sub>2</sub> 3DOM anode<sup>[15a]</sup> in our previous reports. The stable capacity retentions and high-rate capabilities (Figure 8c) are also attractive in practical applications. The full-cell performance shows good ability of sodium storage even at current density as high as  $5000 \text{ mA g}^{-1}$ , and these capacities can be fully recovered when the current density is switched back to  $50 \text{ mA g}^{-1}$ . These results of full cells fully confirm that introducing metal 3DOM current collector holds the potential to build high-rate energy storage devices.

Given the analysis, our observations confirm the possibilities of improving SIB rate performance by tuning the electrical conductivity of electrodes. Although electron transport is magnitudes faster than that of Na ions,<sup>[7b, 23]</sup> strategies to improve electron transport open a novel and efficient avenue to promote rate performance by optimizing fast interface capacitive-like storage rather than comparatively slow bulk storage. The present understandings are expected to not only extent to other sodium-based energy storage device, but also guide the development of functional materials for efficient energy storage at high rates. We are looking forward to more efforts in these open questions in the near future.

### 3. Conclusions

In summary, we have successfully developed an oxide-metal sandwich 3D ordered macroporous architecture (3DOM) as a superior anode candidate for high-rate sodium ion battery (SIB). Taking Ni-TiO<sub>2</sub> sandwich 3DOM as proof-of-concept, anatase TiO<sub>2</sub> delivers a reversible capacity of 233.3 mAhg<sup>-1</sup> in half cells and 210.1 mAh g<sup>-1</sup> in full cells (coupled with P2-Na<sub>2/3</sub>Ni<sub>1/3</sub>Mn<sub>2/3</sub>O<sub>2</sub> cathode) after 100 cycles at 50 mA g<sup>-1</sup>. At the high charge/discharge rate of 5000 mA g<sup>-1</sup>, 104.4 mAh g<sup>-1</sup> in half cells and 68 mAh g<sup>-1</sup> in full cells can also be obtained with satisfied stability, indicating great rate performance of SIBs among various TiO<sub>2</sub>-based anodes. In-depth analysis of electrochemical kinetics fully evidences that the presented remarkable sodium storage ability, in particular at high charge/discharge rates, origins from dominated interface capacitive-like storage because of increased electrical conductivity by introducing of metal 3DOM current collector. The optimized electron transport can efficient accelerate the interface kinetics of sodium storage, and thus improve the interface capacitive-like contribution ratio to the total sodium storage. Fast and stable interface capacitive-like storage efficiently facilitates sodium storage at high rates without huge fading off. Different from the optimized strategies focused on ion diffusion, our observations about employing high electrical conductivity paradigm into electrode design enable a novel and efficient foundation for realizing high-rate SIBs. It is expected to realize a universal design for satisfied energy storage by extending this rule to the secondary ion batteries with other large transport ions. Further combination of ion diffusion optimization holds great promise to attract more research interests in the future development in electrochemical energy storage.

### 4. Experimental Section

*Fabrication of Polystyrene Sphere Colloidal Crystal Templates:* The well-ordered colloidal crystal templates (CCTs) comprised of polystyrene spheres (PSs) were fabricated to form a face-centered cubic packing arrangement using a vertical deposition approach according to our previous works.<sup>[24]</sup> Ti foils as the substrates have been cleaned under sonication by sequentially immersing in acetone (15 min), ethanol (15 min) and distilled water (15 min). The substrates were then immersed vertically in the 0.5 wt% polystyrene latex at 60 °C. Drying of polystyrene latex appears near the Ti foil at very low speed in high moisture. Then, CCTs on Ti foil were heated at 90°C for 5 min and 110 °C for 2 min to enhance the adhesion and avoid crash during the subsequent steps. Here, the diameter of PSs is ~500 nm after optimization of sodium storage ability.

*Fabrication of Ni 3DOM skeletons:* In a typical procedure, 3DOM Ni skeletons were fabricated by electrochemical deposition using an aqueous electrolyte of 1M NiSO<sub>4</sub>•6H<sub>2</sub>O, 0.1M NiCl<sub>2</sub>•6H<sub>2</sub>O and 0.5M H<sub>3</sub>BO<sub>3</sub>. The electrochemical deposition was realized by means of a standard three-electrode system consisting of CCTs as the working electrode, Pt plate as the counter electrode and HgSO<sub>4</sub>/Hg as the reference electrode. Constant current mode with the current of -2.45 mA was used here for 30 minutes by a VSP electrochemical workstation (Bio-Logic, France), where Ni was solidified in-situ at the interstice of CCTs to form a 3DOM architecture. All the depositions were carried out at room temperature. Then, the CCTs were removed by immersing into 10 mL tetrahydrofuran (THF) for 24 h. Ni 3DOM skeletons could be obtained after drying in N<sub>2</sub> flow without any oxidation and kept in N<sub>2</sub>.

*Fabrication of Ni-TiO<sub>2</sub> sandwich 3DOM:* In a typical procedure, TiO<sub>2</sub> were deposited on both sides of Ni 3DOM skeleton by atomic layer deposition (ALD) (PicoSun SUNALE<sup>TM</sup> R-150 ALD system, PicoSun, Finland) to achieve the sandwich construction. Here, TiCl<sub>4</sub> and H<sub>2</sub>O were chosen as the precursors of Ti and O, respectively. TiCl<sub>4</sub> and H<sub>2</sub>O was alternately pulsed

for 0.1 s with separation by 10 s purge of N<sub>2</sub>. The cycle numbers were 400 in order to reach a uniform thickness of 20 nm. The reaction chamber was 70 °C. Then the as-prepared sandwich architectures were annealed in air at 350 °C for 2 h with a ramp rate of 2 °C min<sup>-1</sup> to obtain the anatase phase of TiO<sub>2</sub>.

*Fabrication of TiO<sub>2</sub> 3DOM:* For comparison, TiO<sub>2</sub> 3DOM were also fabricated by ALD on the basis of CCTs instead of Ni 3DOM skeleton with the same settings. To keep the similar ion diffusion length, the repeated cycles are 800 here, which is 2 folds of that of sandwich architectures. The top layer was half-removed by a plasma etching used argon plasma reactor (PDC-32G2) at 70 Pa. Then the as-prepared architectures were also annealed in air at 350 °C for 2 h with a ramp rate of 2 °C min<sup>-1</sup>. Finally, we could obtain anatase TiO<sub>2</sub> 3DOM.

*Fabrication of layered P2-Na<sub>2/3</sub>Ni<sub>1/3</sub>Mn<sub>2/3</sub>O<sub>2</sub>:* Co-precipitation was used to prepare this layered material. Stoichiometric Ni(NO<sub>3</sub>)<sub>2</sub> and Mn(NO<sub>3</sub>)<sub>2</sub> were first mixed with NaOH. Na<sub>2</sub>CO<sub>3</sub> was then added into the mixtures later as the Na source. Collected by centrifugation, the precursors were calcined in air at 600 °C (4 h) and 900 °C (10 h).

*Characterization:* X-ray diffraction (XRD) patterns wererecorded using Cu-K $\alpha$  radiation at 40 kV and 40 mA (SIEMENS/BRUKER D5000 X-ray diffractometer). The scanned range ( $2\theta$ ) is from 20° to 80° with the rate of 0.02° s<sup>-1</sup>. Scanning electron microscopy (SEM) measurement was completed on a Hitachi S4800 field emission scanning microscopy. Transmission electron microscopy (TEM) and energy-dispersive X-ray spectroscopy (EDX) scan measurements were performed on JEM-2010F (JEOL). XPS measurements was performed at the Photoemission Endstation (BL10B) in the National Synchrotron Radiation Laboratory (NSRL) in Hefei, China. All the binding energies were corrected by referencing C 1s to 284.5 eV. Raman spectrum were detected by Raman microscope with a 514.5 nm Ar laser (inVia Ramanmicroscope).

*Electrochemical measurement:* The as-prepared Ni-TiO<sub>2</sub> sandwich 3DOM and TiO<sub>2</sub> 3DOM architectures were directly used as anodes without any conductive additive and polymeric binder. The mass loading of two samples is around 0.76-0.80 mg. So as to cathodes in full-cells, a mixture of 80 % layered P2-Na<sub>2/3</sub>Ni<sub>1/3</sub>Mn<sub>2/3</sub>O<sub>2</sub>, 10% acetylene black and 10 % poly(vinylidene fluoride) (PVDF) by weight was pressed onto an Al foil. Then they were kept at 120 °C for 12 h in vacuum before the assemble of the full-cells. Electrochemical tests were performed through a coin cell configuration (CR2032) with a diameter and thickness of 20 mm and 3.2 mm, respectively, which were assembled in a nitrogen-filled glove box with oxygen and moisture concentrations kept below 0.1 ppm. Sodium metal foil for half-cells and layered P2-Na<sub>2/3</sub>Ni<sub>1/3</sub>Mn<sub>2/3</sub>O<sub>2</sub> for full-cells were used as counter electrodes with separation from the working electrodes by a glass microfiber filter (Whatman, Grade GF/B) with the pore size of 1 μm. The electrolyte used here was 1 mol L<sup>-1</sup> NaClO<sub>4</sub> in propylene carbonate (PC, Aldrich anhydrous 99.7%). All electrochemical measurements were performed at 20 ± 2 °C on a Land CT2001A battery testing system (Land, P. R. China). Cyclic voltammetry (CV), I-V measurement and electrochemical impedance spectroscopy (EIS) were recorded by a VSP electrochemical workstation (Bio-Logic, France). For CV measurement, scan rates were chosen from 0.1 to 5 mV s<sup>-1</sup> in the potential range of 0.01 to 3.0 V (vs. Na/Na<sup>+</sup>). Potential range for I-V is -1 V to 1 V. EIS spectrum were recorded with a frequency range of 100k Hz to 0.1 Hz and a 5 mV AC amplitude.

### **Acknowledgements**

Q. Li, H. Wang and X. Tang contributed equally to this work. The authors acknowledge supports from the National Natural Science Foundation of China (22075263, 52002366), the China Scholarship Council (201408340001), Anhui Provincial Natural Science Foundation

(1808085QB41), the project of Anhui university scientific research (KJ2018A0159), USTC start-up funding (KY2060000165), German Research Foundation (DFG: LE 2249/5-1) and Sino-German Center for Research Promotion (GZ1579), We thank the supports from the Photoemission Endstation (BL10B) in the National Synchrotron Radiation Laboratory (NSRL) in Hefei, China and USTC Center for Micro- and Nanoscale Research and Fabrication. The numerical calculations in this paper have been done on the supercomputing system in the Supercomputing Center of University of Science and Technology of China. We also appreciate Mr. Yue Yang' helps for data processing.

Received: ((will be filled in by the editorial staff))

Revised: ((will be filled in by the editorial staff))

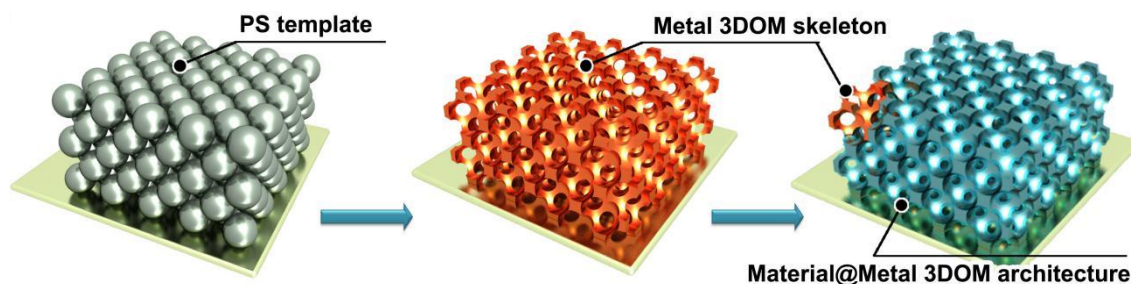
Published online: ((will be filled in by the editorial staff))

## References

- [1] a) J. M. Tarascon, M. Armand, *Nature* **2001**, 414, 359; b) H. P. Zhao, M. Zhou, L. Y. Wen, Y. Lei, *Nano Energy* **2015**, 13, 790; c) M. Zhou, Y. Xu, Y. Lei, *Nano Today* **2018**, 20, 33.
- [2] M. V. Reddy, G. V. S. Rao, B. V. R. Chowdari, *Chem. Rev.* **2013**, 113, 5364.
- [3] a) N. Yabuuchi, K. Kubota, M. Dahbi, S. Komaba, *Chem. Rev.* **2014**, 114, 11636; b) J.-Y. Hwang, S.-T. Myung, Y.-K. Sun, *Chem. Soc. Rev.* **2017**, 46, 3529.
- [4] a) Y. Xu, M. Zhou, Y. Lei, *Mater. Today* **2018**, 21, 60; b) X. Wei, X. Wang, X. Tan, Q. An, L. Mai, *Adv. Funct. Mater.* **2018**, 28, 1804458.
- [5] Y. Xu, M. Zhou, X. Wang, C. L. Wang, L. Y. Liang, F. B. Grote, M. H. Wu, Y. Mi, Y. Lei, *Angew Chem Int Ed* **2015**, 54, 8768.
- [6] X. Xu, J. Liu, J. Liu, L. Ouyang, R. Hu, H. Wang, L. Yang, M. Zhu, *Adv. Funct. Mater.* **2018**, 28, 1707573.
- [7] a) S. Y. Hong, Y. Kim, Y. Park, A. Choi, N.-S. Choi, K. T. Lee, *Energy Environ. Sci.* **2013**, 6, 2067; b) H. Kim, E. Lim, C. Jo, G. Yoon, J. Hwang, S. Jeong, J. Lee, K. Kang, *Nano Energy* **2015**, 16, 62; c) Y. Dou, Y. Wang, D. Tian, J. Xu, Z. Zhang, Q. Liu, B. Ruan, J. Ma, Z. Sun, S. X. Dou, *2D Mater.* **2017**, 4, 015022.

- [8] a) M. Zhou, Y. Xu, J. X. Xiang, C. L. Wang, L. Y. Liang, L. Y. Wen, Y. G. Fang, Y. Mi, Y. Lei, *Adv. Energy Mater.* **2016**, 6, 1600448; b) Z. Wei, D. Wang, X. Yang, C. Wang, G. Chen, F. Du, *Adv. Mater. Interfaces* **2018**, 5, 1800639.
- [9] a) Z. Le, F. Liu, P. Nie, X. Li, X. Liu, Z. Bian, G. Chen, H. B. Wu, Y. Lu, *ACS Nano* **2017**, 11, 2952; b) T. Brezesinski, J. Wang, J. Polleux, B. Dunn, S. H. Tolbert, *J. Am. Chem. Soc.* **2009**, 131, 1802; c) G. Longoni, R. L. Pena Cabrera, S. Polizzi, M. D'Arienzo, C. M. Mari, Y. Cui, R. Ruffo, *Nano Lett* **2017**, 17, 992; d) Y. Zhu, L. Peng, D. Chen, G. Yu, *Nano Lett* **2016**, 16, 742.
- [10] a) P. Simon, Y. Gogotsi, *Nat. Mater.* **2008**, 7, 845; b) V. Augustyn, J. Come, M. A. Lowe, J. W. Kim, P. L. Taberna, S. H. Tolbert, H. D. Abruna, P. Simon, B. Dunn, *Nat. Mater.* **2013**, 12, 518.
- [11] a) V. Augustyn, P. Simon, B. Dunn, *Energy Environ. Sci.* **2014**, 7, 1597; b) T. Brousse, D. Belanger, J. W. Long, *J. Electrochem. Soc.* **2015**, 162, A5185.
- [12] L. Y. Wen, M. Zhou, C. L. Wang, Y. Mi, Y. Lei, *Adv. Energy Mater.* **2016**, 6, 1600468.
- [13] L. Kavan, *J. Solid State Electrochem.* **2014**, 18, 2297.
- [14] J. Ye, A. C. Baumgaertel, Y. M. Wang, J. Biener, M. M. Biener, *ACS Nano* **2015**, 9, 2194.
- [15] a) M. Zhou, Y. Xu, C. Wang, Q. Li, J. Xiang, L. Liang, M. Wu, H. Zhao, Y. Lei, *Nano Energy* **2017**, 31, 514; b) Y. Xu, E. M. Lotfabad, H. Wang, B. Farbod, Z. Xu, A. Kohandehghan, D. Mitlin, *Chem. Comm.* **2013**, 49, 8973.
- [16] a) Z. G. N. a. G. C. Chaofeng Liu, *Mater. Today* **2016**, 19, 109; b) C. J. Chen, Y. W. Wen, X. L. Hu, X. L. Ji, M. Y. Yan, L. Q. Mai, P. Hu, B. Shan, Y. H. Huang, *Nat Commun* **2015**, 6, 6929.
- [17] a) K. Tang, L. Fu, R. J. White, L. Yu, M.-M. Titirici, M. Antonietti, J. Maier, *Adv. Energy Mater.* **2012**, 2, 873; b) A. L. M. Reddy, S. R. Gowda, M. M. Shaijumon, P. M. Ajayan, *Adv. Mater.* **2012**, 24, 5045; c) Y. Xu, C. Zhang, M. Zhou, Q. Fu, C. Zhao, M. Wu, Y. Lei, *Nat Commun* **2018**, 9, 1720; d) C. Vaalma, D. Buchholz, M. Weil, S. Passerini, *Nat. Rev. Mater.* **2018**, 3, 18013.
- [18] a) G. Longoni, R. L. P. Cabrera, S. Polizzi, M. D'Arienzo, C. M. Mari, Y. Cuo, R. Ruffo, *Nano Lett.* **2017**, 17, 992; b) Y. Zhang, Z. Y. Ding, C. W. Foster, C. E. Banks, X. Q. Qiu, X. B. Ji, *Adv. Funct. Mater.* **2017**, 27, 1700856; c) J. F. Ni, S. D. Fu, Y. F. Yuan, L. Ma, Y. Jiang, L. Li, J. Lu, *Adv. Mater.* **2018**, 30, 1704337.
- [19] a) M. Zhou, J. Bao, M. S. Tao, R. Zhu, Y. Q. Zeng, Z. W. Wei, Y. Xie, *Chem. Commun.* **2012**, 48, 3439; b) M. Wu, Y. Wang, Y. Xu, J. Ming, M. Zhou, R. Xu, Q. Fu, Y. Lei, *ACS Appl. Mat. Interfaces* **2017**, 9, 23647; c) Y. Xu, M. Zhou, L. Y. Wen, C. L. Wang, H. P. Zhao, Y. Mi, L. Y. Liang, Q. Fu, M. H. Wu, Y. Lei, *Chem. Mater.* **2015**, 27, 4274.
- [20] H. Li, X. Huang, L. Chen, *J. Power Sources* **1999**, 81-82, 340.
- [21] a) J. Wang, J. Polleux, J. Lim, B. Dunn, *J. Phys. Chem. C* **2007**, 111, 14925; b) T. Brezesinski, J. Wang, S. H. Tolbert, B. Dunn, *Nat. Mater.* **2010**, 9, 146; c) P. Simon, Y. Gogotsi, B. Dunn, *Science* **2014**, 343, 1210.

- [22] a) V. Augustyn, J. Come, M. A. Lowe, J. W. Kim, P.-L. Taberna, S. H. Tolbert, H. D. Abruna, P. Simon, B. Dunn, *Nat. Mater.* **2013**, 12, 518; b) T. Brezesinski, J. Wang, S. H. Tolbert, B. Dunn, *Nat. Mater.* **2010**, 9, 146.
- [23] L.F. Que, F.D. Yu, Z.B. Wang, D.M. Gu, *Small* **2018**, 14, 1704508.
- [24] a) M. Zhou, H. Wu, J. Bao, L. Liang, X. Lou, Y. Xie, *Angew Chem Int Ed* **2013**, 52, 8579; b) M. Zhou, J. Bao, Y. Xu, J. Zhang, J. Xie, M. Guan, C. Wang, L. Wen, Y. Lei, Y. Xie, *ACS Nano* **2014**, 8, 7088.



**Scheme 1.** Schematic illustration of the fabrication of sandwich 3DOMs by atomic layer deposition (ALD) assisted colloidal crystal template (CCT) method.

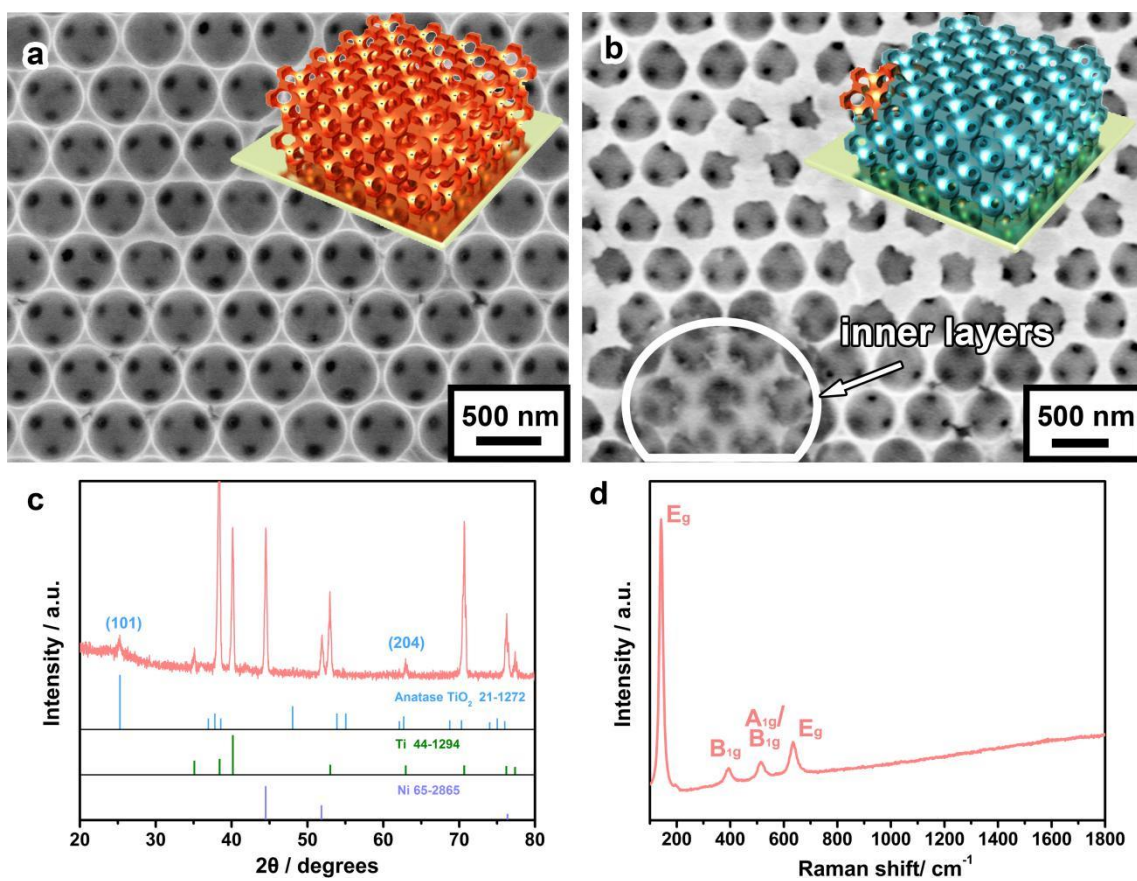


**Figure 1.** Characterizations of Ni-TiO<sub>2</sub> sandwich 3DOM. (a,b) SEM images of the Ni 3DOM skeleton (a) and Ni-TiO<sub>2</sub> sandwich 3DOM (b); (c) XRD pattern of Ni-TiO<sub>2</sub> sandwich 3DOM; (d) Raman spectra of Ni-TiO<sub>2</sub> sandwich 3DOM.

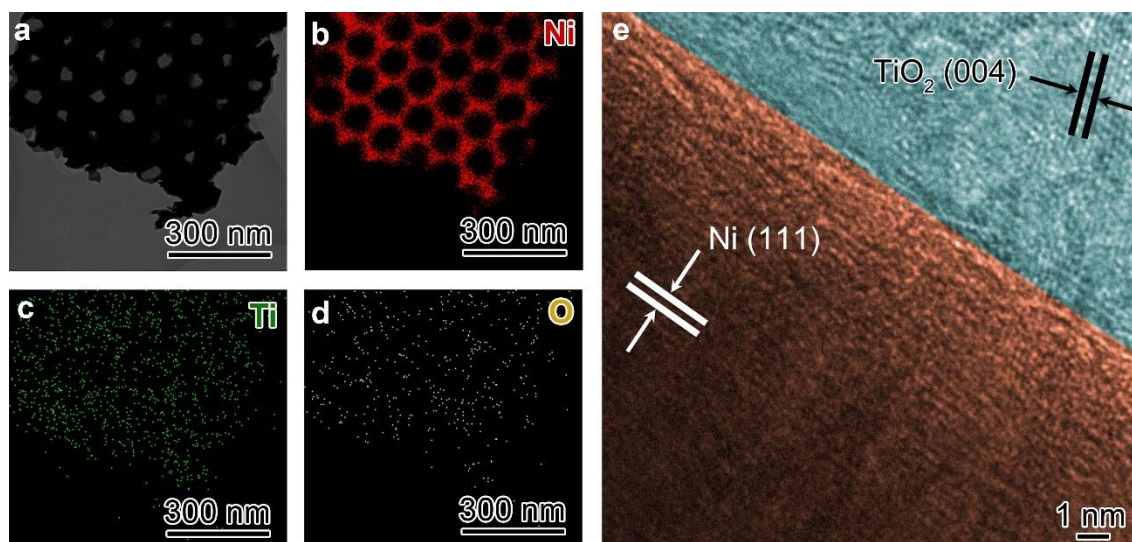


**Figure 2.** TEM analysis of Ni-TiO<sub>2</sub> sandwich 3DOM. (a) TEM image; (b-d) Elemental distribution of Ni, Ti, and O across Ni-TiO<sub>2</sub> sandwich 3DOM; (e) HRTEM image of interface between Ni and TiO<sub>2</sub>, indicating the direct and clean contact of Ni and TiO<sub>2</sub>.

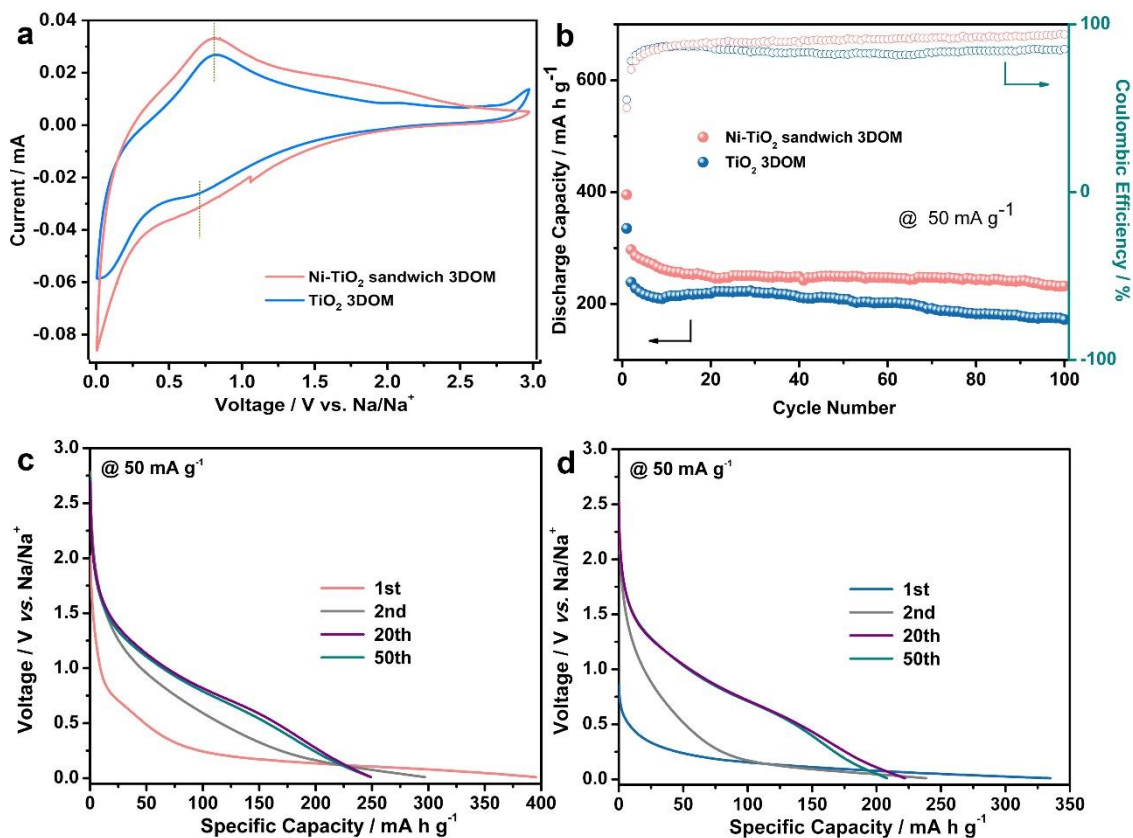


**Figure 3.** (a) Current-voltage characteristics at the scan rate of 0.1 mV s<sup>-1</sup> within the potential range of 0.01-3.0 V of Ni-TiO<sub>2</sub> sandwich 3DOM and pure TiO<sub>2</sub> 3DOM electrodes. The mass loadings of the two samples are similar; (b) Cycling performance of the Ni-TiO<sub>2</sub> sandwich 3DOM and TiO<sub>2</sub> 3DOM; (c,d) Discharge profiles of the Ni-TiO<sub>2</sub> sandwich 3DOM(c) and TiO<sub>2</sub> 3DOM (d) at the current density of 50 mA g<sup>-1</sup>.

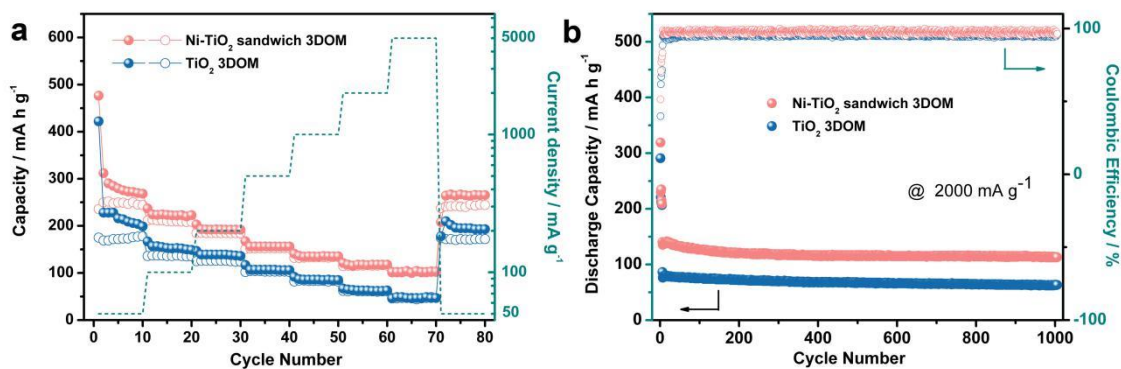
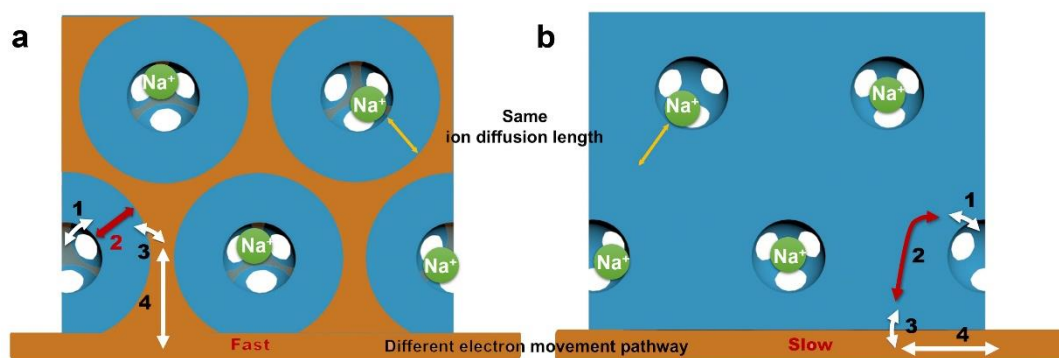


**Figure 4.** (a) The rate performance of Ni-TiO<sub>2</sub> sandwich 3DOM and TiO<sub>2</sub> 3DOM for SIBs with current densities varying from 50 mA g<sup>-1</sup> to 5000 mA g<sup>-1</sup>; (b) The cycling stability of Ni-TiO<sub>2</sub> sandwich 3DOM and TiO<sub>2</sub> 3DOM at 2000 mA g<sup>-1</sup> for 1000 cycles.



**Scheme 2.** Schematic illustration of the ion diffusion length and electron transport pathways in Ni-TiO<sub>2</sub> sandwich 3DOM (a) and TiO<sub>2</sub> 3DOM (b). Blue stands for TiO<sub>2</sub>, while orange represents Ni. The yellow arrays stand for ion diffusion. The white and red arrays are four major electron movement events occurring during ion-intercalation and deintercalation. (1) accumulation and/or reaction at the electrode/electrolyte interface; (2) electron transport throughout the active materials; (3) electron injection and extraction at the electrode-current collector interface; (4) electron transport in current collector.

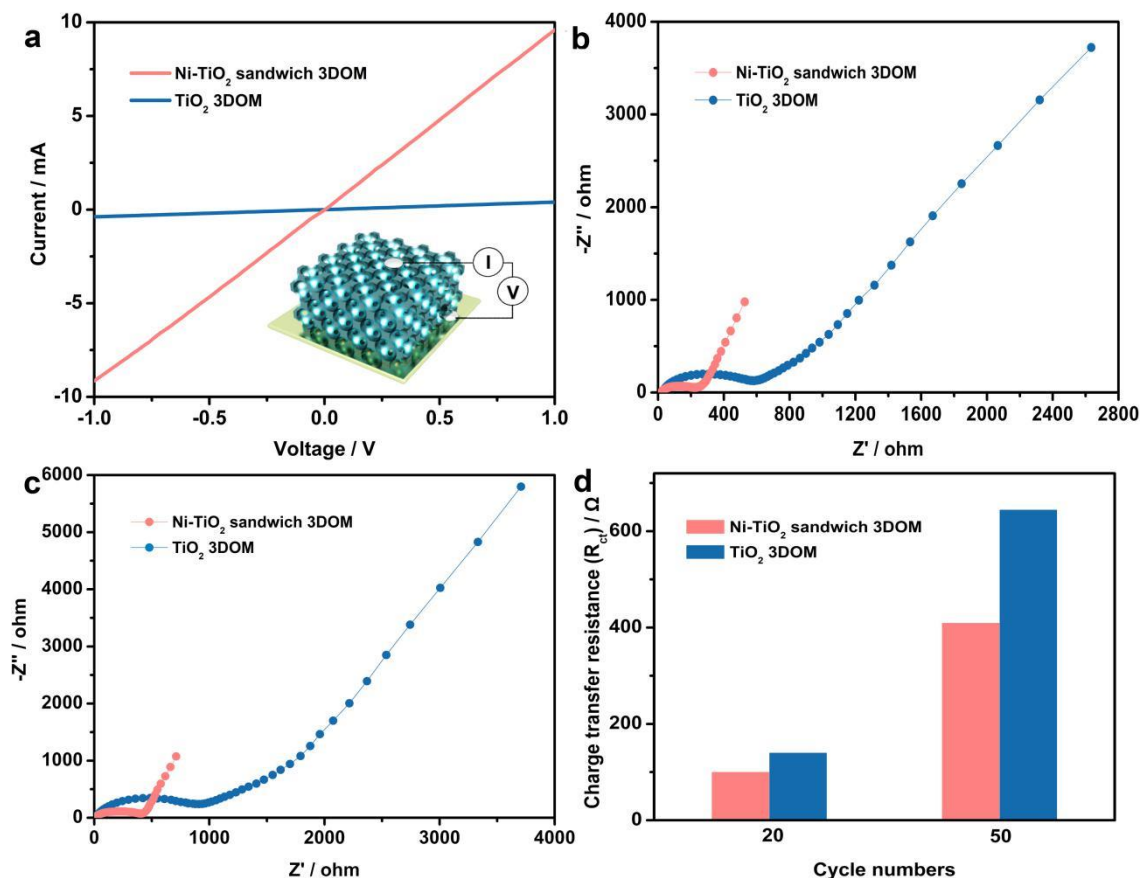


**Figure 5.** (a) Resistance from current-voltage (I-V) characteristics. Diagrammed in inset of (a) is the schematic view of the testing devices; (b,c) Nyquist plots of electrochemical impedance of Ni-TiO<sub>2</sub> sandwich 3DOM and TiO<sub>2</sub> 3DOM electrodes for SIBs at 50 mA g<sup>-1</sup> after different cycles: (b) 20 cycles, (c) 50 cycles; (d) Comparison of charge transfer resistance (R<sub>ct</sub>) of both kinds of electrodes after 20 and 50 cycles.

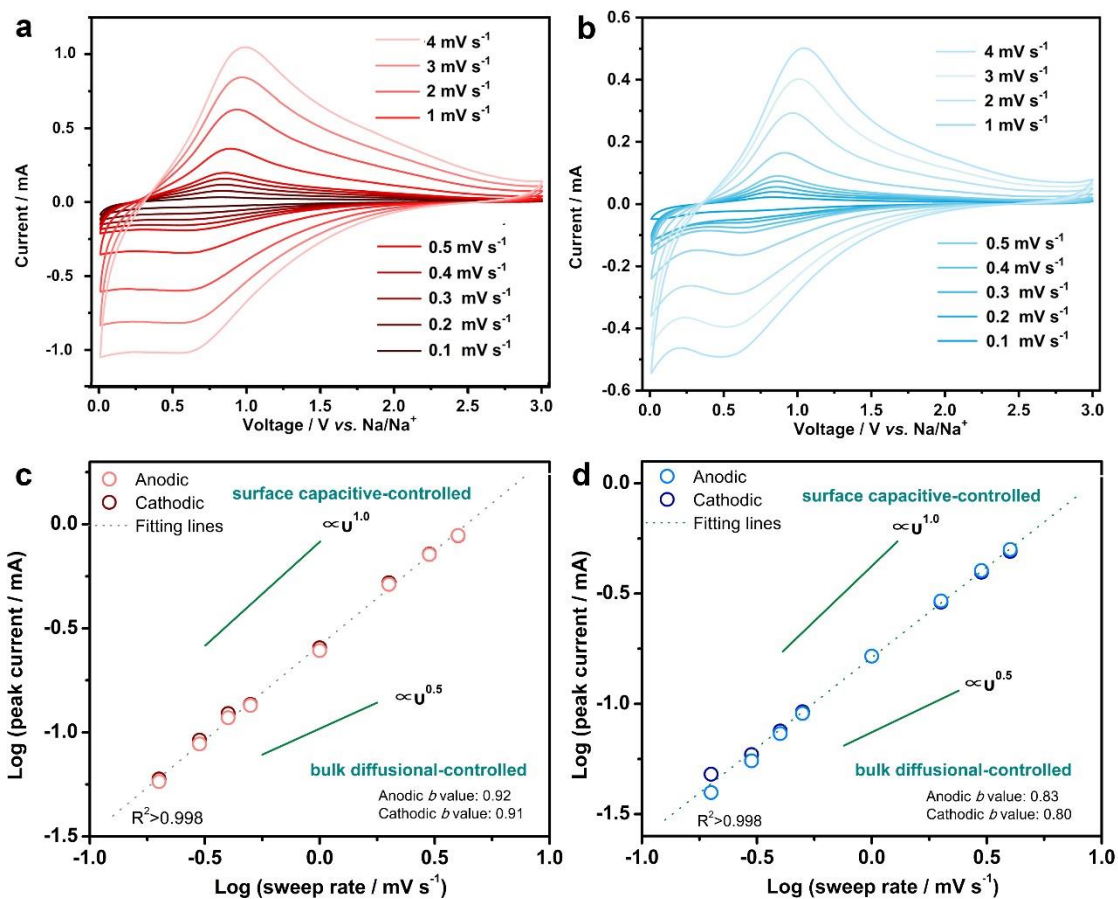


**Figure 6.** Kinetics analysis of electrochemical behaviors. (a,b) Current-voltage characteristics at sweep rates from 0.1 to 5 mV s<sup>-1</sup> of Ni-TiO<sub>2</sub> sandwich 3DOM (a) and TiO<sub>2</sub> 3DOM (b); (c,d) Determination of *b*-values on the basis of peak currents and scan rates: Ni-TiO<sub>2</sub> sandwich 3DOM (c) and TiO<sub>2</sub> 3DOM (d).

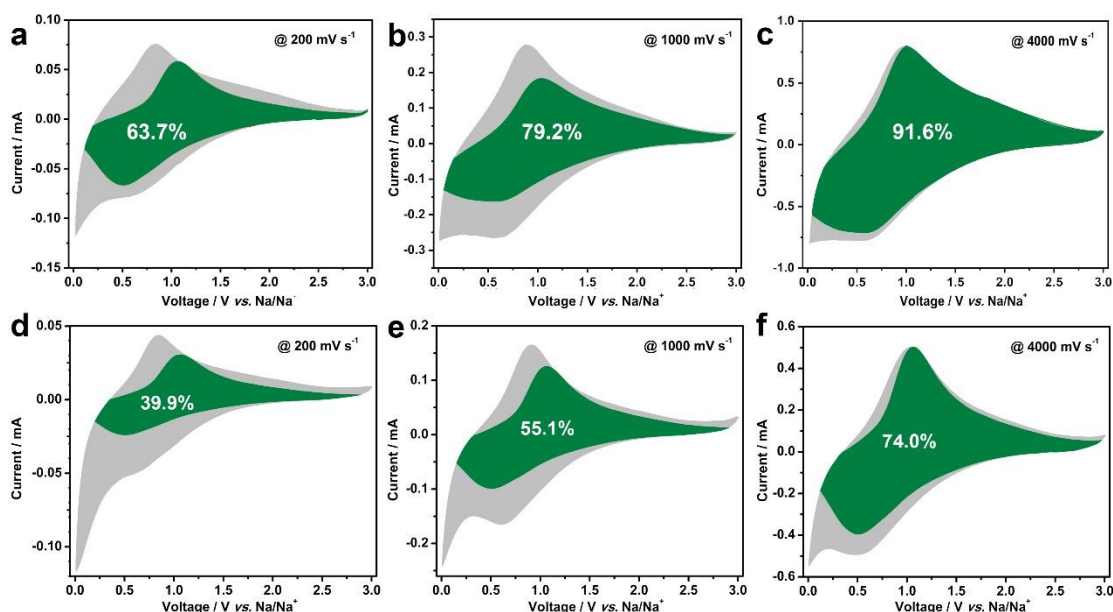


**Figure 7.** Separation of the capacitive-like and diffusion controlled currents of Ni-TiO<sub>2</sub> sandwich 3DOM (a-c) and TiO<sub>2</sub> 3DOM (d-f) at various sweep rates: (a,d) 0.2 mV s<sup>-1</sup>; (b,e) 1 mV s<sup>-1</sup>; (c,f) 4 mV s<sup>-1</sup>.

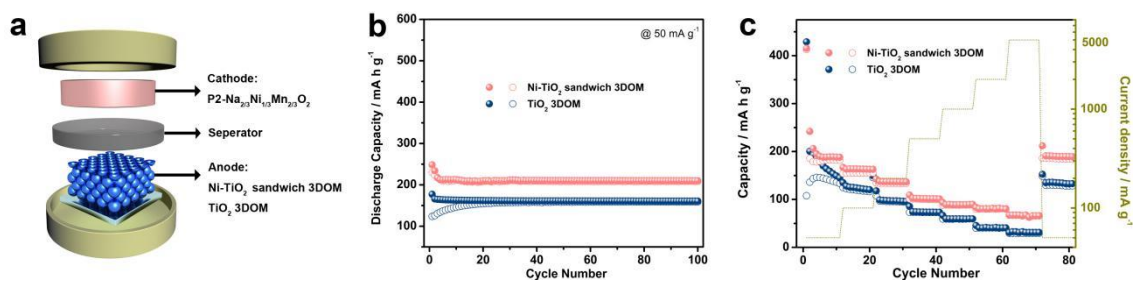


**Figure 8.** (a) Scheme of a two-electrode full cell with TiO<sub>2</sub> sandwich 3DOM and TiO<sub>2</sub> 3DOM anodes and P2-Na<sub>2/3</sub>Ni<sub>1/3</sub>Mn<sub>2/3</sub>O<sub>2</sub> cathode; (b) Cycling performance at 50 mA g<sup>-1</sup>; (c) Rate performance with current densities varying from 50 to 5000 mA g<sup>-1</sup>.

**Electrical** conductivity adjustment is employed to enhance the interface capacitive-like storage towards high-rate sodium storage. Superior rate capabilities and stable retention are achieved in return for this design in both half-cells and full-cells. This understanding is expected for a universal design to realize satisfied energy storage using large transport ions.

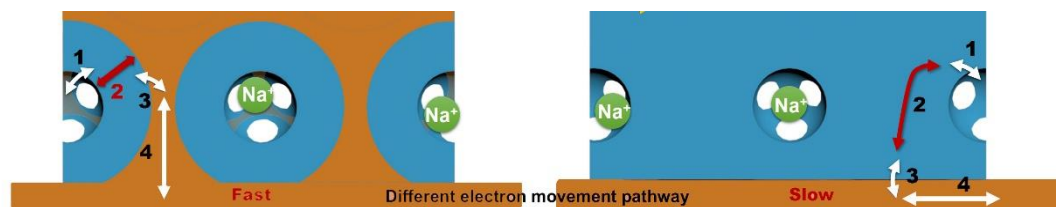
### Keyword

sandwich architecture, 3D current collector, electrical conductivity, interface capacitive-like storage, sodium ion battery

*Qianwen Li, Hang Wang, Xinfeng Tang, Min Zhou<sup>\*</sup>, Huaping Zhao, Yang Xu, Wei Xiao, Yong Lei<sup>\*</sup>*

### Electrical Conductivity Adjustment for Interface Capacitive-like Storage in Sodium-ion Battery

ToC figure



## Supporting Information

### **Electrical Conductivity Adjustment for Interface Capacitive-like Storage in Sodium-ion Battery**

*Qianwen Li, Hang Wang, Xinfeng Tang, Min Zhou\*, Huaping Zhao, Yang Xu, Wei Xiao, Yong Lei\**

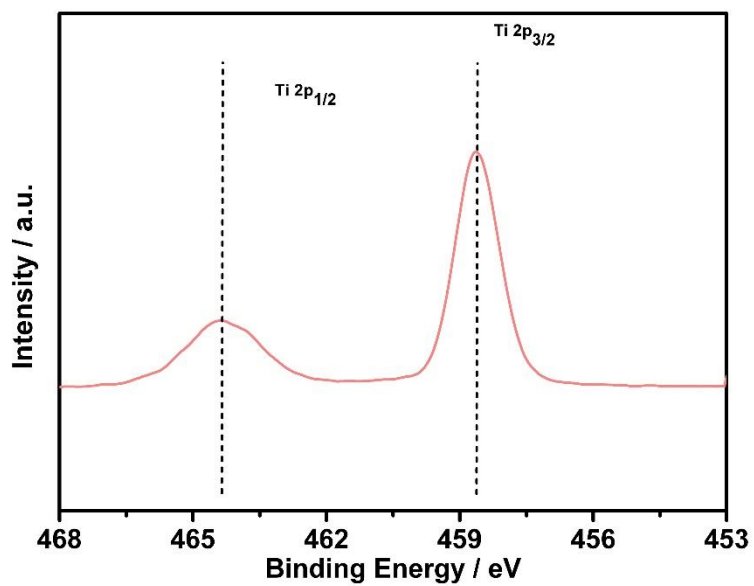


Figure S1. XPS data of Ni-TiO<sub>2</sub> sandwich 3DOM.

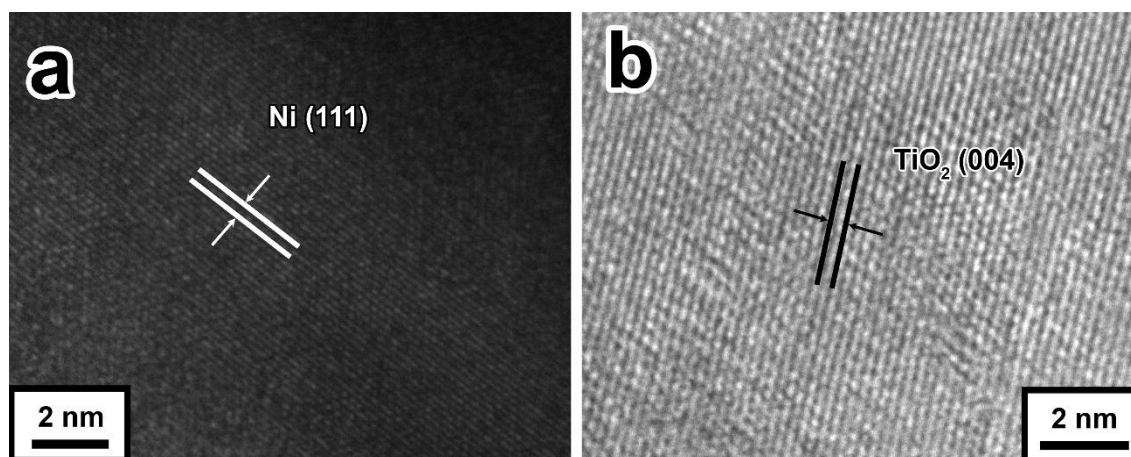
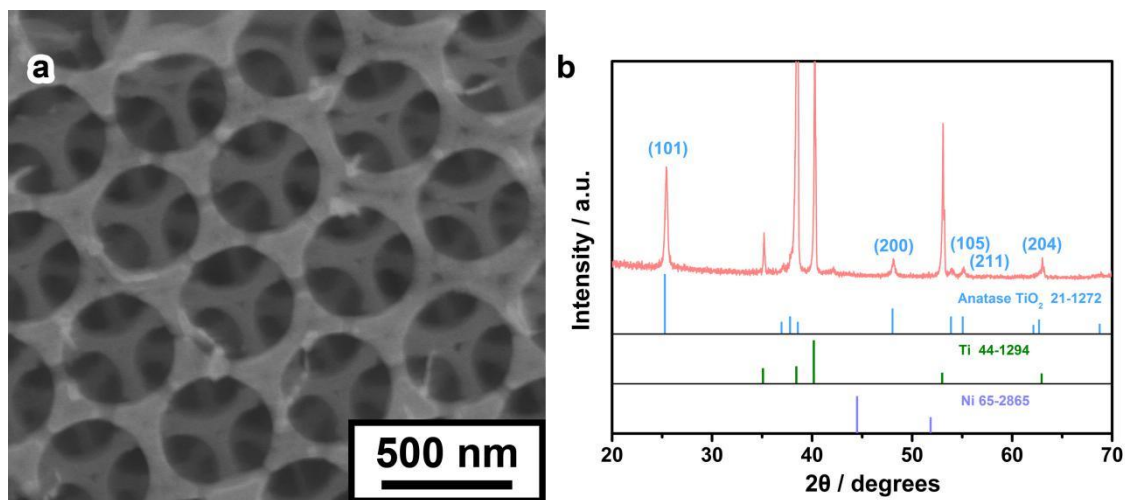
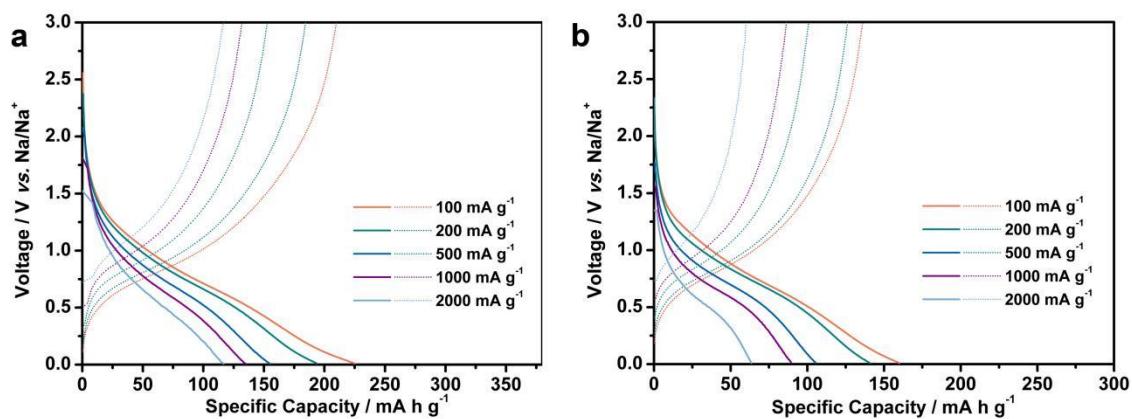


Figure S2. HRTEM images of Ni and TiO<sub>2</sub>.



**Figure S3.** Characterizations of TiO<sub>2</sub> 3DOM. (a) SEM image; (b) XRD pattern.



**Figure S4.** The voltage plateau profiles of Ni-TiO<sub>2</sub> sandwich 3DOM (a) and TiO<sub>2</sub> 3DOM (b) for SIBs at elevated rates from 50 mA g<sup>-1</sup> to 2000 mA g<sup>-1</sup>.

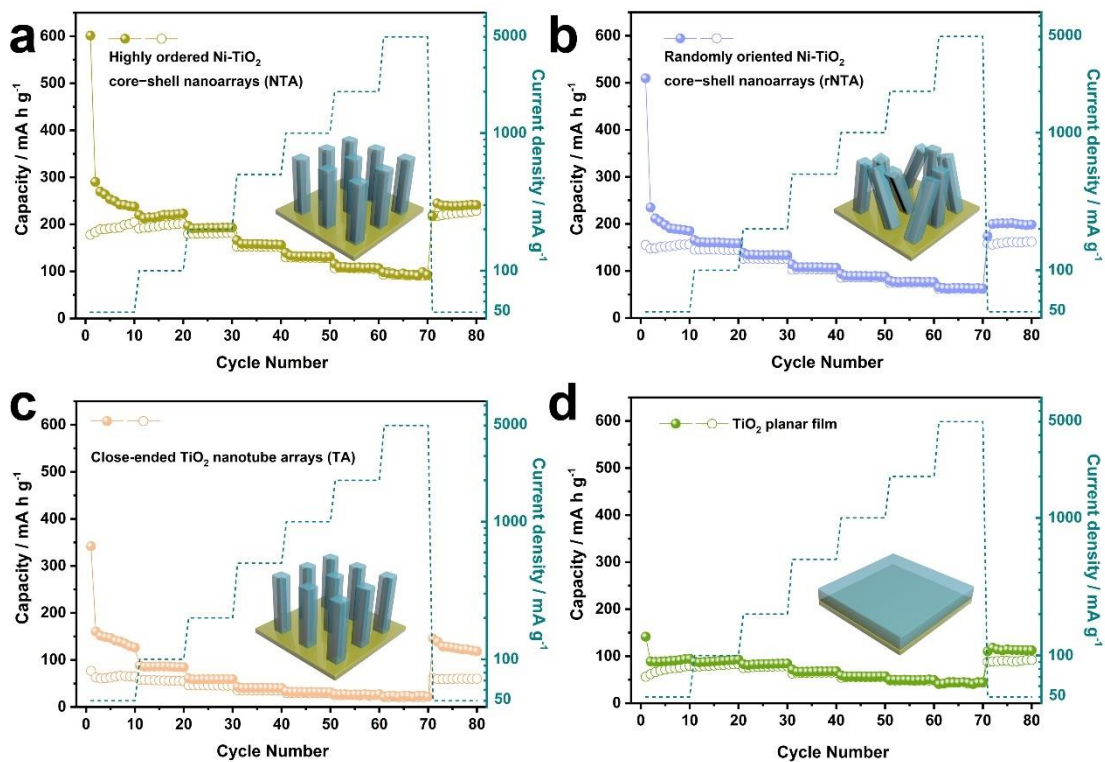


**Figure S5.** The rate performance of various  $\text{TiO}_2$ -based electrodes for SIBs with different geometries of current collectors. (a) highly ordered Ni- $\text{TiO}_2$  core-shell nanowire array (NTA);  
[7] (b) randomly oriented Ni- $\text{TiO}_2$  nanowire array (rNTA); [7] (c) half-closed  $\text{TiO}_2$  nanotube array (TA); [7] (d) planar  $\text{TiO}_2$ .

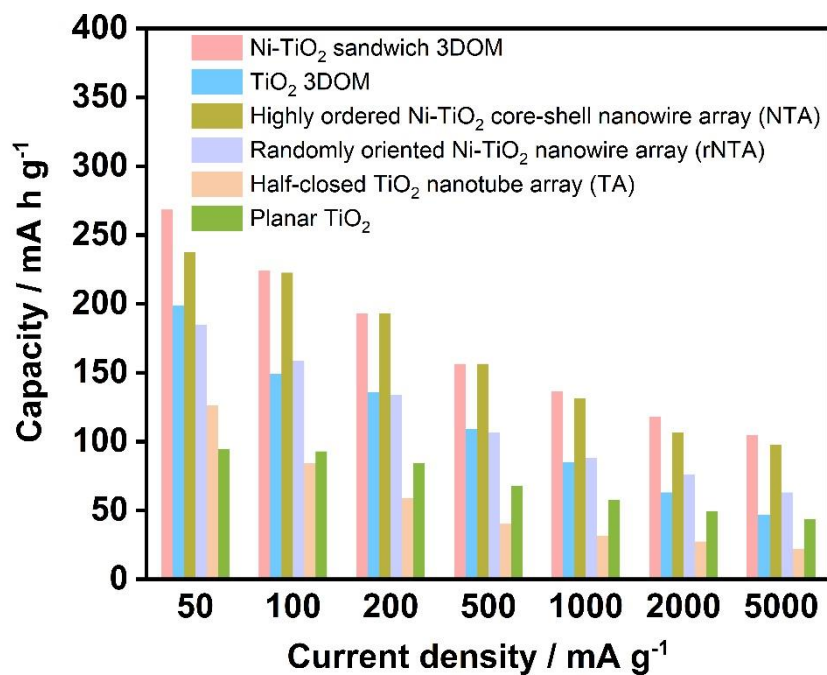


**Figure S6.** Comparisons of rate performance among various TiO<sub>2</sub>-based electrodes for SIBs with different geometries of current collectors.<sup>[7]</sup>

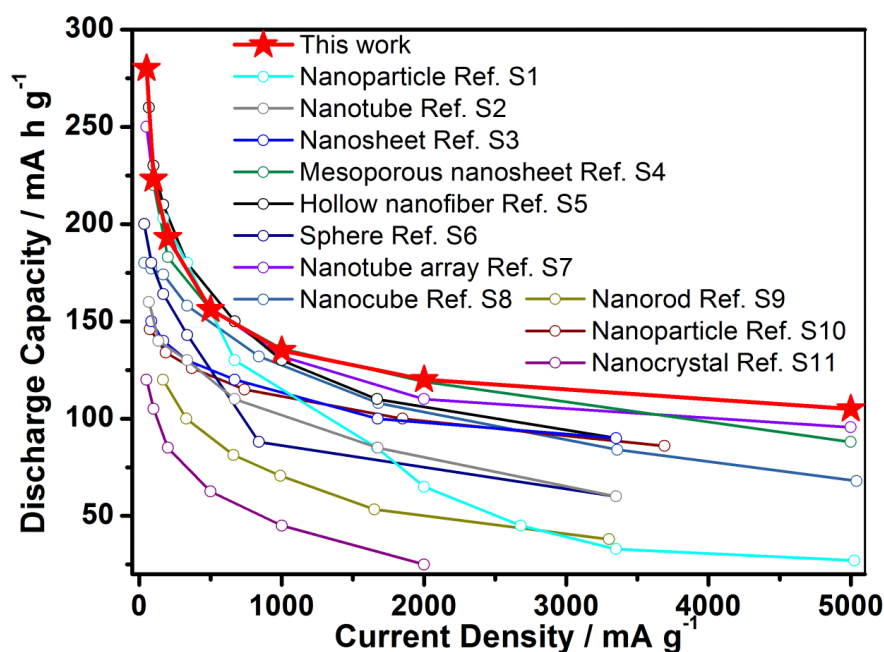


**Figure S7.** Comparisons of rate performance among Ni-TiO<sub>2</sub> sandwich 3DOM and other reported pure TiO<sub>2</sub>-based anodes. These data are estimated from the figures of rate performance in literatures except Ref. S8 and Ref. S10.

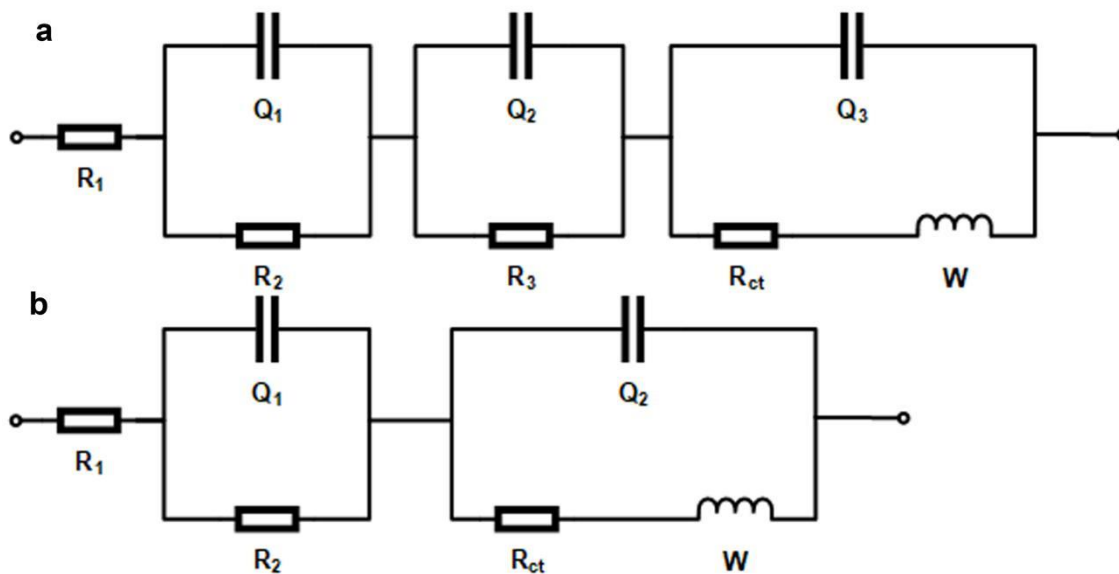


**Figure S8.** Equivalent circuit of Ni-TiO<sub>2</sub> sandwich 3DOM (a) and TiO<sub>2</sub> 3DOM (b).

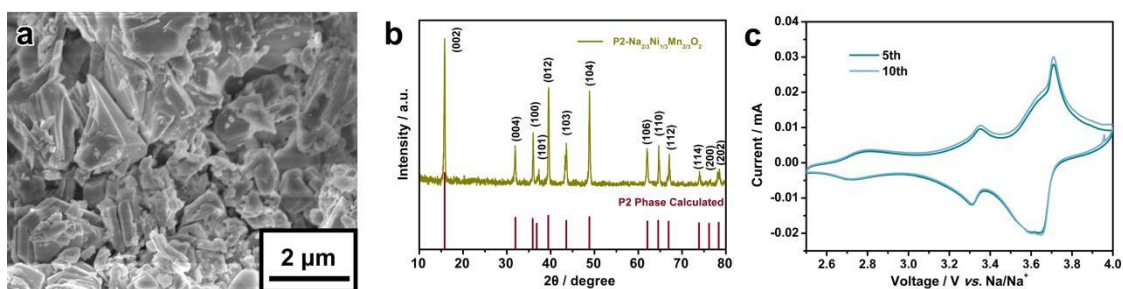


**Figure S9.** Characterizations and electrochemical performance of P2-Na<sub>2/3</sub>Ni<sub>1/3</sub>Mn<sub>2/3</sub>O<sub>2</sub> cathodes. (a) Typical SEM of image; (b) XRD pattern; (c) Cyclic voltammograms curves at scan rate of 0.5 mV s<sup>-1</sup>.

**Table S1.** Electrochemical performance comparison of Ni-TiO<sub>2</sub> sandwich 3DOM anodes for sodium ion batteries with previously reported anatase TiO<sub>2</sub>-based anodes.

<i>Material</i>	<i>Current density</i> <i>/ mA g<sup>-1</sup></i>	<i>Cycle</i>	<i>Capacity</i> <i>/ mAh g<sup>-1</sup></i>	<i>Current density</i> <i>/ mA g<sup>-1</sup></i>	<i>Cycle</i>	<i>Capacity</i> <i>/ mAh g<sup>-1</sup></i>	<i>Reference</i>
<i>Ni-TiO<sub>2</sub> sandwich 3DOM</i>	50	100	233	2000	1000	109	<i>This work</i>
<i>3DOM</i>	50	100	175	2000	1000	63	<i>This work</i>
<i>Nanoparticle</i>	167	100	150	/	/	/	<i>S1</i>
<i>Nanotube</i>	67	350	156	6700	/	33	<i>S2</i>
<i>Nanosheet</i>	167	450	140	670	2000	120	<i>S3</i>
<i>Mesoporous nanosheet</i>	100	100	199	10000	10000	44	<i>S4</i>
<i>Hollow nanofiber</i>	67	300	200	3350	2000	90	<i>S5</i>
<i>Sphere</i>	168	200	166	840	/	70	<i>S6</i>
<i>Nanotube array</i>	50	100	115	5000	/	30	<i>S7</i>
<i>Nanocube</i>	33.6	10	180	1680	1000	108	<i>S8</i>
<i>Nanorod</i>	10	100	145	1650	50	18	<i>S9</i>
<i>Nanoparticle</i>	36.9	60	135	1850	1000	100	<i>S10</i>
<i>Nanocrystal</i>	50	100	150	2000	/	38	<i>S11</i>

<b>Nanobelts arrays</b>	50	100	154	/	/	/	S12
<b>Nanorod</b>	2000	20	140	5000	60	53	S13
<b>urchin-like morphology</b>	84	200	167	3360	5000	77	S14
<b>Nanoparticle</b>	100	200	69	1600	10	16 <sup>a</sup>	S15
<b>core-shell TiO<sub>2</sub> Sphere</b>	100	200	124	1000	2000	108	S16
<b>Nanosheet</b>	100	100	225	5000	10	25 <sup>a</sup>	S17
<b>Nanoparticle</b>	33.5	50	101	1675	10	22 <sup>a</sup>	S18
<b>Nanoparticle</b>	335	1000	178	670	10	55 <sup>a</sup>	S19
<b>Nanocrystal</b>	670	200	139	5360	2000	83	S20
<b>Porous nanocrystal</b>	335	10	120 <sup>a</sup>	1675	1000	33	S21
<b>Nanotube arrays</b>	200	500	78	/	/	/	S22
<b>Nanotube arrays</b>	335	45	164	3350	1000	100	S23
<b>Nanotube arrays</b>	50	250	70	1000	10	10 <sup>a</sup>	S24
<b>Nanotube arrays</b>	168	100	216	5000	10	25 <sup>a</sup>	S25

a: Capacity is estimated from the images of rate capability.

## Reference

- [1] Y. Zhang, W. Hong, Y. Zhang, W. Xu, Z. Shi, X. Li, H. Hou, X. Ji, *Electrochim. Acta*

- 2018**, 283, 1514.
- [2] W. Wei, M. Valvo, K. Edstrom, L. Nyholm, *Chemelectrochem* **2018**, 5, 674.
- [3] B. Li, B. Xi, Z. Feng, Y. Lin, J. Liu, J. Feng, Y. Qian, S. Xiong, *Adv. Mater.* **2018**, 30, 1705788.
- [4] K. Lan, Y. Liu, W. Zhang, Y. Liu, A. Elzatahry, R. Wang, Y. Xia, D. Al-Dhayan, N. Zheng, D. Zhao, *J. Am. Chem. Soc.* **2018**, 140, 4135.
- [5] Y. Wu, Y. Jiang, J. Shi, L. Gu, Y. Yu, *Small* **2017**, 13, 1700129.
- [6] Y. Li, S. Wang, Y. B. He, L. K. Tang, Y. V. Kaneti, W. Lv, Z. Q. Lin, B. H. Li, Q. H. Yang, F. Y. Kang, *J. Mater. Chem. A* **2017**, 5, 4359.
- [7] Y. Xu, M. Zhou, L. Wen, C. Wang, H. Zhao, Y. Mi, L. Liang, Q. Fu, M. Wu, Y. Lei, *Chem. Mater.* **2015**, 27, 4274.
- [8] X. Yang, C. Wang, Y. Yang, Y. Zhang, X. Jia, J. Chen, X. Ji, *J. Mater. Chem. A* **2015**, 3, 8800.
- [9] K.T. Kim, G. Ali, K. Y. Chung, C. S. Yoon, H. Yashiro, Y.-K. Sun, J. Lu, K. Amine, S.T. Myung, *Nano Lett.* **2014**, 14, 416.
- [10] L. Wu, D. Buchholz, D. Bresser, L. G. Chagas, S. Passerini, *J. Power Sources* **2014**, 251, 379.
- [11] Y. Xu, E. M. Lotfabad, H. Wang, B. Farbod, Z. Xu, A. Kohandehghan, D. Mitlin, *Chem. Comm.* **2013**, 49, 8973.
- [12] Y. Yang, Q. Fu, H. Zhao, Y. Mi, W. Li, Y. Dong, M. Wu, Y. Lei, *J. Alloys Compd.* **2018**, 769, 257.
- [13] F. Liu, X. Sun, Y. Liu, X. Song, J. Gao, G. Qin, *Appl. Surf. Sci.* **2019**, 473, 873.
- [14] Q. Gan, H. He, K. Zhao, Z. He, S. Liu, S. Yang, *ACS Appl. Mater. Interfaces* **2018**, 10, 7031.
- [15] J. Chen, E. Wang, J. Mu, B. Ai, T. Zhang, W. Ge, L. Zhang, *J. Mater. Sci.* **2019**, 54, 592.
- [16] Y. Bai, R. Xarapatgvl, X. Wu, X. Liu, Y. Liu, K. Wang, J. Chen, *Nanoscale*, **2019**, 11, 17860.
- [17] J. Ma, M. Xing, L. Yin, K. San, K. Hui, *Appl. Surf. Sci.* **2021**, 536, 147735.
- [18] X. Bai, T. Li, U. Gulzar, E. Venezia, L. Chen, S. Monaco, Z. Dang, M. Prato, S. Marras, P. Salimi, S. Fugattini, C. Capiglia, Z. Proietti, R. Zaccaria, *Nanoscale*, **2020**, 12, 15896.
- [19] Q. Ni, R. Dong, Y. Bai, Z. Wang, H. Ren, S. Sean, F. Wu, H. Xu, C. Wu, *Energy Storage Mater.* **2020**, 25, 903.
- [20] B. Chen, Y. Meng, F. Xie, F. He, C. He, K. Davey, N. Zhao, S. Qiao, *Adv. Mater.* **2018**, 30, 1804116.
- [21] G. Zhang, C. Chu, J. Yang, C. Tung, Y. Wang, *J. Phys. Chem. C* **2019**, 123, 7025.

- [22] J. Yang, Z. Chen, H. Wang, F. Liang, R. Chen, R. Wu, *Mater. Lett.* **2017**, 207, 149.
- [23] J. Ni, S. Fu, Y. Yuan, L. Ma, Y. Jiang, L. Li, J. Lu, *Adv. Mater.* **2018**, 30, 1704337.
- [24] G. Cha, S. Mohajernia, N. T. Nguyen, A. Mazare, N. Denisov, I. Hwang, P. Schmuki, *Adv. Energy Mater.* **2020**, 10, 1903448.
- [25] G. Liu, M. Huang, Z. Zhang, B. Xi, H. Li, S. Xiong, *J. Energy Chem.* **2021**, 53, 175.